Ferroelectricity Improvement in Ultra-Thin Hf0.5Zr0.5O2 Capacitors by the Insertion of a Ti Interfacial Layer

Greta Segantini, Rabei Barhoumi, Benoît Manchon, Ingrid Cañero Infante, Pedro Rojo Romeo, Matthieu Bugnet, Nicolas Baboux, Shruti Nirantar, Damien Deleruyelle, Sharath Sriram, et al.

RESEARCH ARTICLES

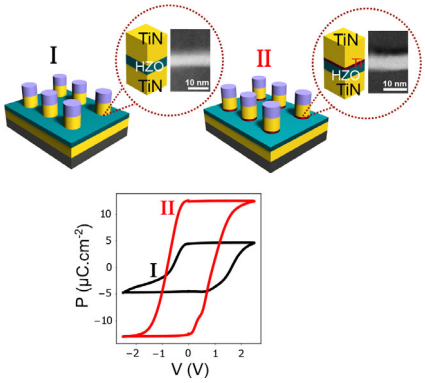

Interface engineering of ferroelectric hafnium zirconium oxide (HZO)-based devices is crucial to improve their electrical performances and their scalability. Here, the insertion of an ultra-thin titanium layer at the electrode/HZO interface drastically increases the remnant polarization of 6 nm thick HZO-based capacitors. The thickness of the interfacial layer proved to be a parameter of interest to account for the phenomena occurring at the electrode/HZO/electrode interfaces.

physica status solidi pss rrl
www.pss-rapid.com

Ferroelectricity Improvement in Ultra-Thin $Hf_{0.5}Zr_{0.5}O_2$ Capacitors by the Insertion of a Ti Interfacial Layer

Greta Segantini,* Rabei Barhoumi, Benoît Manchon, Ingrid Cañero Infante, Pedro Rojo Romeo, Matthieu Bugnet, Nicolas Baboux, Shruti Nirantar, Damien Deleruyelle, Sharath Sriram, and Bertrand Vilquin

The effect at the nanoscale of a Ti interfacial layer on the performances of TiN/$HfZrO_2$/TiN capacitors is reported. Ferroelectric hafnium zirconium oxide, HZO, is synthesized by magnetron sputtering of a $Hf_{0.5}Zr_{0.5}O_2$ ceramic target. Titanium nitride top and bottom electrodes are grown by reactive magnetron sputtering. The insertion of an ultra-thin Ti layer at the top electrode/HZO interface impacts the crystalline phase and the electrical properties of the ferroelectric HZO. Following post-deposition annealing, the Ti layer is oxidized and becomes titanium oxide. Compositional and structural characterization is performed using glancing incidence X-Ray diffraction and electron energy-loss spectroscopy. The TiO_z layer is clearly distinguishable at the top electrode/HZO interface. Electrical characterization is conducted by positive-up-negative-down (PUND) technique. The remnant polarization reaches a maximum value of 25 μC cm^{-2} for 6 nm thick HZO. The results are discussed in the framework of structural, compositional, and physical properties of the electrode/HZO interfaces and their effect on the electrical performances of thin HZO-based junctions, which could subsequently be considered for the demonstration of synaptic learning mechanisms for neuromorphic applications.

1. Introduction

The discovery of ferroelectricity in hafnium oxide (HfO_2) by Böscke et al.,[1,2] in 2011, paved the road for the development of a wide range of concepts and devices based on ferroelectric HfO_2. Since then, HfO_2 has been demonstrated to be a very promising material for the realization of ferroelectric field-effect transistors (FeFET), ferroelectric random access memory (FRAM), negative capacitance field-effect transistors (NCFET), and ferroelectric tunnel junctions (FTJs) for neuromorphic devices.[3] Different chemical substitutions and processing conditions have been explored to stabilize ferroelectric polymorphs, based on HfO_2, in polycrystalline thin films. Among different strategies, which exploit compounds from the solid solution of the physically and chemically compatible zirconium oxide (ZrO_2) and HfO_2, the Hf:Zr 1:1 substitution compound is of particular interest,[4,5] due to its high polarization value. For instance, $Hf_{0.5}Zr_{0.5}O_2$ (HZO) has shown robust ferroelectricity and low-temperature preparation, which is a crucial aspect for its integration into the semiconductor-based industry. The low crystallization temperature of the ferroelectric phase guarantees the compatibility of HZO with the complementary metal–oxide–semiconductor process. Among HfO_2/HZO-based nonvolatile memory devices, FTJs offer the possibility to increase the device scalability for their integration into dense memory arrays.[6] HZO-based FTJs have also been considered promising for the implementation of synaptic devices for neuromorphic computing.[7] A FTJ is a trilayer stack where a thin ferroelectric material, which serves as a tunnel barrier,[8] is sandwiched between two electrodes. In the literature, several examples of FTJs based on electrode–ferroelectric–electrode structure for memory applications have been reported.[7,9] In the present work, we compare the structural and electrical characteristics of an electrode-ferroelectric-electrode stack with those of an electrode–ferroelectric–metal–electrode structure. In the former, a thin layer of HZO is sandwiched between a titanium nitride (TiN) bottom (BE) and top electrode (TE), while in the latter, an ultra-thin layer of titanium (Ti) is inserted at the TE/HZO interface. This type of structure has previously been reported. Max et al.[10] developed a

G. Segantini, R. Barhoumi, B. Manchon, I. Cañero Infante, P. Rojo Romeo, M. Bugnet, N. Baboux, D. Deleruyelle, B. Vilquin
Univ Lyon
Ecole Centrale Lyon
INSA Lyon
UCBL
CPE Lyon
CNRS
INL
UMR5270
69130 Ecully, France
E-mail: greta.segantini@ec-lyon.fr

G. Segantini, S. Nirantar, S. Sriram
Functional Materials and Microsystems Research Group and Micro Nano Research Facility
RMIT University
Melbourne, Australia

The ORCID identification number(s) for the author(s) of this article can be found under https://doi.org/10.1002/pssr.202100583.

DOI: 10.1002/pssr.202100583

TiN/HZO/Al_2O_3/TiN stack, where Al_2O_3 serves as a tunnel barrier and the HZO film provides the ferroelectric switching. Shekhawat et al.[11] reduced the voltage of read and write operations of HZO-based FTJs by integrating a 1 nm-thick Al_2O_3 interfacial layer. Qi et al.[12] demonstrated that the incorporation of a TiO_2 layer at the bottom and top interface of a TiN/HZO/TiN stack increases the amount of orthorhombic phase in as-deposited HZO. Gaddam et al.[13] showed that dielectric–ferroelectric–dielectric capacitors based on HZO exhibit good ferroelectric properties even at low annealing temperatures. Finally, Ryu et al. proposed an Al_2O_3/HZO-based structure, which shows a synaptic behavior, where the Al_2O_3 layer enables a sizeable tunnel electroresistance ratio.[14] The synthesis of HZO films less than 8 nm thick that exhibit robust ferroelectricity is a challenging task.[15] In this work, we significantly improve the ferroelectric properties of a few nm thick HZO films, by inserting an ultra-thin metallic interfacial layer. We demonstrate outstanding remnant polarization and high endurance in 6 nm thick non-epitaxial HZO. The obtained results show that by means of interface engineering it is possible to scale the thickness of HZO down to a few nm, without compromising its ferroelectricity. This would be of great interest for FTJ applications. The heterostructure fabrication was entirely performed by radio-frequency magnetron sputtering.[16] Subsequently, we investigated the effect of a Ti interfacial layer of different thicknesses on the crystalline phase, electronic structure, and electrical performances of 6 nm thick HZO-based capacitors. We propose an optimized stack with enhanced ferroelectric properties.

2. Experimental Section

2.1. Synthesis

The growth of the stack was performed on n^+Si(100) substrates. Prior to deposition, the substrates were cleaned with acetone and ethanol, and freed from the native oxide layer by a buffer oxide etching procedure. The depositions of the hafnium zirconium oxide (HZO) layer, TiN bottom and top electrodes, and Ti/Pt top electrical contacts were realized by magnetron sputtering at room temperature, using an AC-450 sputtering machine by Alliance Concept. The 50 nm thick TiN electrodes were grown by radio-frequency reactive magnetron sputtering of a Ti target at a pressure of 5×10^{-3} mbar, using a mixture of Ar and N_2. The 6 nm thick HZO layer was grown by magnetron sputtering of a $Hf_{0.5}Zr_{0.5}O_2$ ceramic target at a pressure of 5×10^{-2} mbar.[16–18] Afterward, UV photolithography (20 mW cm^{-2} at a wavelength of 405 nm) was performed to obtain the electrical contacts, made by a few nm thick Ti adhesive layer and 50 nm of Pt. The photoresist used for the lithography process was a positive photoresist and the exposure time was 5 s. Once synthesized, the stack was subjected to rapid thermal annealing at a temperature of 450 °C, for 30 s, in an N_2 atmosphere. **Figure 1** shows the structure of the synthesized samples. Figure 1a,b reports the structure of the specimen without (1a) and with (1b) the insertion of the Ti layer, together with the scanning transmission electron microscope (STEM) high-angle annular dark-field (HAADF) image of the TE/HZO/BE cross-section. Figure 1c shows the optical image of the surface of the sample with the pattern of capacitors.

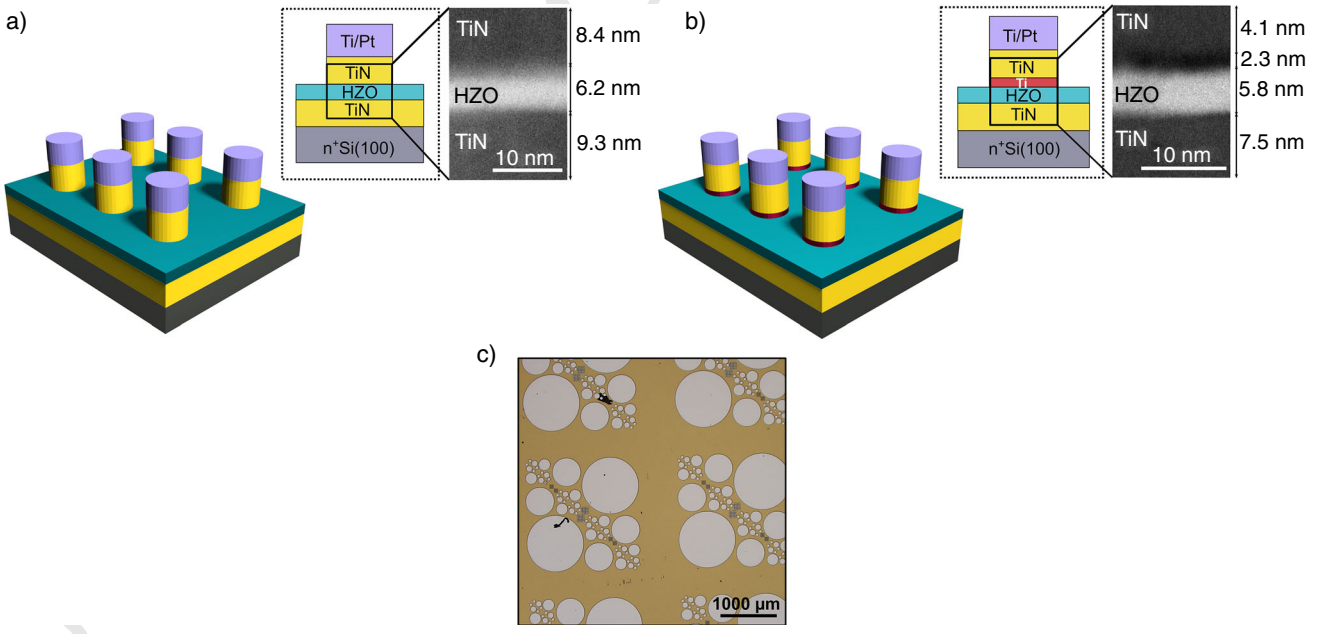

Figure 1. Schematic of the structure of the samples. a) n^+Si/TiN/HZO/TiN/Ti/Pt, on the right is the scanning transmission electron microscope- high-angle annular dark field (STEM-HAADF) image of the TE/HZO/BE cross-section. b) n^+Si/TiN/HZO/Ti/TiN/Ti/Pt, on the right is the STEM-HAADF image of the TE/HZO/BE cross-section. c) Optical image of the surface of the sample with the pattern of capacitors used for the electrical characterization.

Table 1. Film growth conditions.

		Sputtering Process		
Target-substrate distance		8 cm		
Base pressure		$<5 \times 10^{-7}$ mbar		
Ignition pressure		5×10^{-2} mbar		
Deposited elements	**TiN**	$Hf_{0.5}Zr_{0.5}O_2$	**Ti**	**Pt**
Substrate	n^+Si(100)	n^+Si(100)/TiN	n^+Si(100)/TiN/HZO	n^+Si(100)/TiN/HZO/TiN
Target (purity)	Ti (99 995%)	ZrO_2/HfO_2 (50%/50%)	Ti(99 995%)	Pt (99.95%)
Target RF power/voltage [w/v]	300 W	100 W	100 W	137 V
Holder DC bias voltage [V]	60 V	None	None	None
Gas [sccm]	Ar 50 sccm; N_2 3 sccm	Ar 50 sccm	Ar 50 sccm	Ar 50 sccm
Working pressure [mbar]	5×10^{-3} mbar	5×10^{-2} mbar	5×10^{-2} mbar	5×10^{-3} mbar
Deposition rate	≈5 nm min	≈4 nm min	≈3.5 nm min	≈17 nm min
		UV Lithography Conditions		
Photoresist		Positive AZ5214		
Exposure time [s]		5 s		
Flood exposure time [s]		25 s		
Power per units area [mW cm^{-2}]		20 mW cm^{-2} at 405 nm		
		Rapid Thermal Annealing Conditions		
Temperature [°]		450 °C		
Atmosphere (1 atm)		N_2		
Time [s]		30 s		

Growth, annealing, and capacitor fabrication conditions are reported in **Table 1**.

2.2. Characterization

The thickness of the layers composing the stacks was evaluated by X-Ray reflectometry (XRR) and their structural characterization was performed by glancing incidence X-Ray diffraction (GI-XRD) by means of a six-circle goniometer SmartLab Rigaku diffractometer using a 9 kW copper rotating anode. GI-XRD experiments were carried out using a parabolic multilayer mirror for parallel beam setting, Ni filter for Cu K alpha radiation selection, 0.114° aperture parallel slit analyzer, and a 0D scintillating counter. The composition and the electronic structure in the vicinity of the top interface (TE/HZO) were investigated by electron energy-loss spectroscopy (EELS) in STEM mode. The instrument used was a Jeol JEM-ARM200F NeoARM transmission electron microscope, equipped with a high-brightness cold-FEG, a CEOS ASCOR aberration-corrector of the probe forming lenses, a Gatan imaging filter quantum, and operated at 200 kV. The cross-section specimen for STEM analysis was prepared by the Ga-focused ion beam (FIB) milling technique. Core-loss STEM-EELS data were collected using the spectrum-imaging technique implemented in the Gatan microscopy suite, with a dispersion of 0.3 eV/channel. Polarization versus voltage measurements were carried out at room temperature on 20 μm-diameter capacitors, using a Keithley 4200A-SCS semiconductor parameter analyzer. The electrical characterization was performed using a manual probe station, where samples were kept in a closed environment and electrical contact was made with two tungsten-tip probes. The voltage was applied by contacting the top electrode of each device with one probe, while the other was kept on the common bottom electrode. $P-V$ characteristics were obtained by positive-up-negative-down (PUND) technique, which consists of a train of five pulses. A negative reset pulse is applied to initialize the polarization along one direction, subsequently two positive (P and U) and two negative pulses (N and D) are applied. The PUND pulses had a triangular shape, with an amplitude of 2.5 V and a rising/falling time of 50 μs. The endurance test was performed by cycling the capacitors, usually until the breakdown.

3. Results and Discussion

3.1. Structural Characterization by GI-XRD and EELS

Four samples, labeled Samples 0, 1, 2, and 3 for simplicity, were studied. For Sample 0, the HZO layer was sandwiched between TiN bottom and top electrodes, while for Samples 1, 2, and 3 an ultra-thin layer of Ti, of 1, 2, and 3 nm, respectively, was deposited at the top interface by RF magnetron sputtering. The GI-XRD patterns obtained for the four samples are shown in **Figure 2**. Reference XRD patterns for TiN, HZO *o*-/*t*-phase, and HZO *m*-phase from ICDD00-038-1420, ICDD01-083-0808, and ICDD00-034-0104, respectively, were considered to fit the experimental pattern for each sample, and are overlaid in

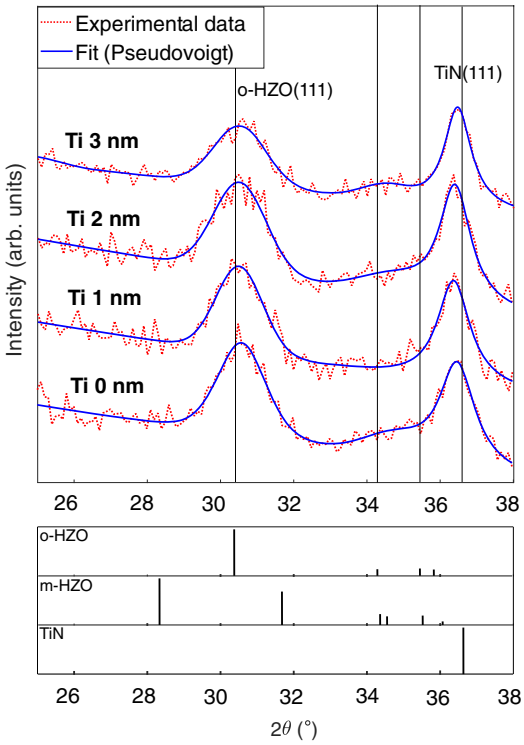

Figure 2. Glancing incidence X-Ray diffraction (GI-XRD) patterns that show the intensity versus scattering angle of the four considered samples. Starting from the bottom: Sample 0—n^+Si/TiN/HZO/TiN/Ti/Pt, Ti 0 nm, Sample 1—n^+Si/TiN/HZO/Ti/TiN/Ti/Pt, Ti 1 nm, Sample 2—n^+Si/TiN/HZO/Ti/TiN/Ti/Pt, Ti 2 nm, Sample 3—n^+Si/TiN/HZO/Ti/TiN/Ti/Pt, Ti 3 nm. Below, the expected peak positions for orthorhombic HZO, monoclinic HZO, and TiN. For the fit, only the position of Cu K alpha 1 has been considered.

Figure 2. The dotted red line represents the experimental data and the straight blue line shows the fitted curve. The fitting function is a pseudo-Voigt that accounts for the Cu K alpha 1 and K alpha 2 radiations. The position of the *o*-/*t*- peak at ≈30.5°, which corresponds to (111) planes, coincides with the expected value.[19] No *m*-phase components at ≈28.4° (*m*-HZO (11-1)), and at ≈31.6°(*m*-HZO(111)) were detected. The intensity of *o*-/*t*-peak, which is similar for the four cases, is not correlated to the presence of the Ti layer nor to its thickness. This analysis validates the existence of the ferroelectric *o*-HZO phase for the analyzed samples. The diffraction peak of the *o*-HZO(111) family of planes, at ≈30.5°, was considered for the evaluation of the average crystalline size of the HZO layer by means of the Scherrer equation.[20] Overall, crystalline sizes around 5 nm were found for all samples. Details of the calculation are shown in the Supplemental Material. The crystalline size is not correlated to the thickness of the Ti interfacial layer.

The structure and composition of the TiN/HZO top interface in Sample 0 and the Ti/HZO top interface in Sample 2 were investigated at the nanoscale by STEM-EELS on pristine capacitors of 10 μm diameter, as shown in **Figure 3 and 4**, respectively. The spatial distribution of N (N–K edge at ≈400 eV), Ti (Ti-$L_{2,3}$ edges at ≈455 eV), and O (O–K edge at ≈530 eV) across the TE/HZO interfaces are shown in Figure 3a and 4a. For the TiN/HZO top interface of Sample 0, a TiN(O) layer is evidenced from the simultaneous presence of the N–K, Ti-$L_{2,3}$, and O–K edges, resulting from the oxidation of the TiN layer. This oxidation is localized over ≈2 nm, as indicated by the O–K edge fine structures, which decreases consistently from HZO to TiN, and is accompanied by a shift of the O–K edge onset to lower energy, as shown in Figure 3d. The TiN oxidation phenomenon is also described in previous work by our group[17] in a structure synthesized in the same experimental conditions as the ones considered in this work. The N–K edge fine structures in the TiN layer are similar to the ones reported in the literature,[21] with

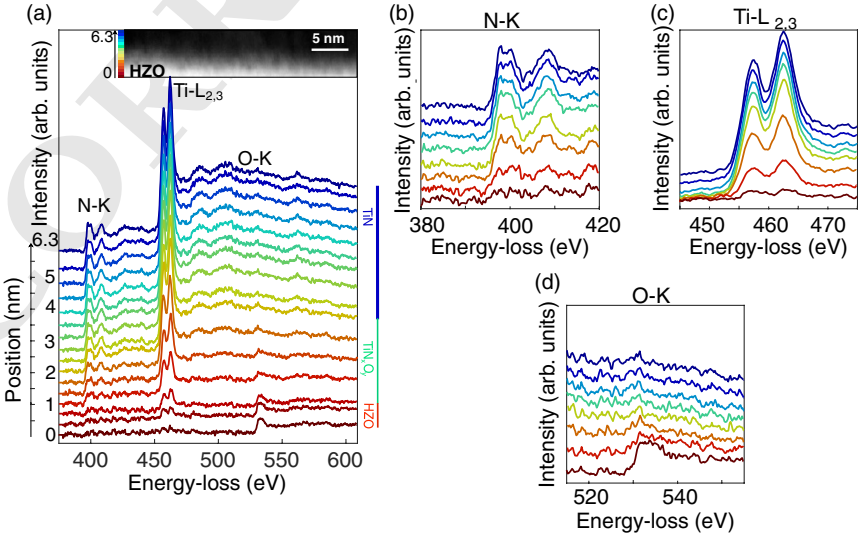

Figure 3. STEM- electron energy-loss spectroscopy (EELS) analysis of Sample 0. a) EELS spectra acquired across the TE/HZO interface. Each spectrum is the average of 81 spectra projected horizontally along the interface, and is shifted vertically for clarity. The HAADF image acquired simultaneously is shown in the inset. A spectrum image dataset of 16 × 81 pixels was acquired with a step size of 3.9Å, over an area of ≈ 6.3 × 32 nm^2. b), c), d) Display over a narrower energy range of the N–K, Ti-$L_{2,3}$, and O–K edges, respectively.

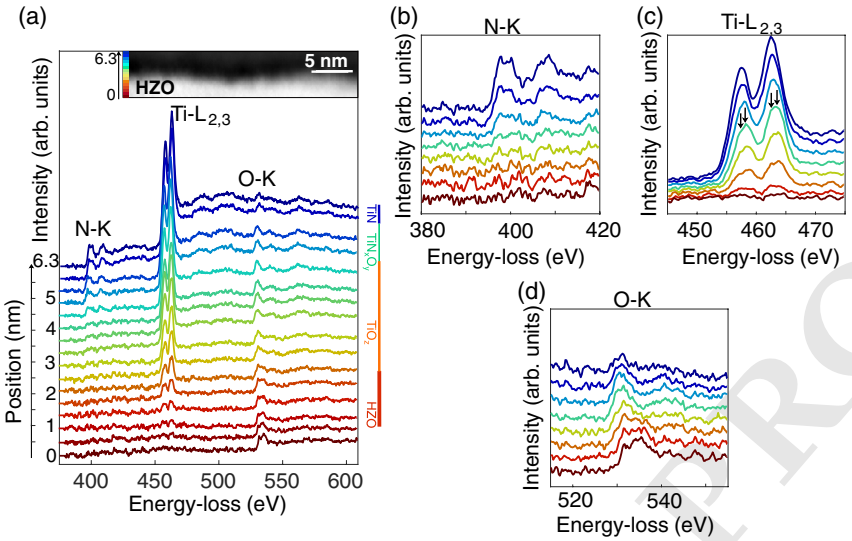

Figure 4. STEM-EELS analysis of Sample 2. a) EELS spectra acquired across the TE/HZO interface. Each spectrum is the average of 81 spectra projected horizontally along the interface, and is shifted vertically for clarity. The HAADF image acquired simultaneously is shown in the inset. A spectrum image dataset of 16 × 81 pixels was acquired with a step size of 3.9Å, over an area of ≈ 6.3 × 32 nm^2. b), c), d) Display over a narrower energy range of the N–K, Ti-$L_{2,3}$, and O–K edges, respectively.

some fine structure variations and an overall decrease of the N–K edge intensity in the TiN(O) layer, potentially resulting from oxidation[22] (Figure 3b). In addition, the constant energy and shape of the Ti-$L_{2,3}$ fine structures across the interface, shown in Figure 3c, suggest a low oxidation. For the Ti/HZO top interface of Sample 2, a TiO_z layer is evidenced over a couple of nanometers, from the simultaneous presence of the O–K and Ti-$L_{2,3}$ edges and the absence of the N–K edge, as shown in Figure 4a,b, thus indicating the oxidation of the Ti layer. Specifically, the Ti-$L_{2,3}$ fine structures split (Figure 4c), as expected in TiO_2, where the L_3 and L_2 peaks split under the influence of the crystal field.[23] The L_3 and L_2 peaks also shift to higher energy compared to TiN. The O-K edge fine structures change across the HZO/TiO_z interface, and the edge onset shifts to lower energy in the TiN(O) layer, as shown in Figure 4d. The TiN layer deposited on top of Ti is thus partially oxidized over a very narrow range, as exemplified from the simultaneous presence of N–K, Ti-$L_{2,3}$, and O–K edges. The N–K edge fine structures at the Ti/TiN interface are different from TiN, as a result of oxidation and subsequent chemical bonding between Ti *d* and O *p* states. Finally, the O–K near edge structures of HZO are different in both samples. In Sample 2 (Figure 4d), two distinct peaks are visible within 10 eV above the edge onset, as expected in HZO polymorphs,[24,25] contrary to Sample 0 (Figure 3d). The near-edge structures reflect the local electronic structure around O atoms, which are covalently bonded to Hf and Zr atoms. Several parameters could be the cause of these spectral variations, such as local changes of the crystal field,[26] the presence of oxygen vacancies,[27–30] or local inhomogeneities in Hf versus Zr content[31] integrated over in the spectra displayed in Figure 3 and 4. The origin of these differences at the O–K edge in both HZO layers is still under investigation. The EELS analysis demonstrates that the Ti layer is fully oxidized (Sample 2), whereas in the absence of Ti, the TiN layer is only partially oxidized. The oxygen redistribution induced by the Ti layer is meant to produce oxygen vacancies inside the HZO film by pulling oxygen atoms toward the top interface. The oxidation phenomenon of the Ti layer explains the contrast difference at the TE/HZO interface in the cross-sectional HAADF images in Figure 1a,b. In Sample 2, the TE/HZO interface appears dark from the presence of the TiO_z interfacial layer.

3.2. Electrical Characterization by PUND

Polarization (*P*) versus applied voltage (*V*) measurements were performed on the four samples at room temperature (300 K). **Figure 5** shows the $P - V$ curves after 10^4 cycles of Samples

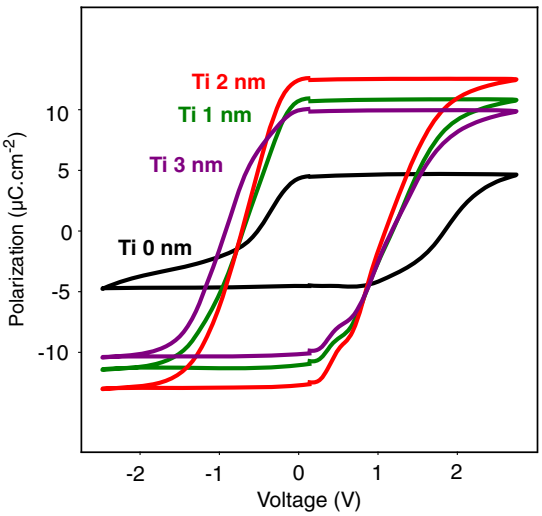

Figure 5. Electrical characterization for Samples 0, 1, 2, and 3: *P–V* curves taken on woken up capacitors after 10^4 cycles.

Table 2. Values of remnant polarization in $\mu C\,cm^{-2}$ for samples 0, 1, 2, and 3 for the pristine state, after 10^4 cycles, and before breakdown.

	Pristine	After 10^4 cycles	Before breakdown
Sample 0 (Ti 0 nm)	0	10	9
Sample 1 (Ti 1 nm)	9	23	25
Sample 2 (Ti 2 nm)	10	25	30
Sample 3 (Ti 3 nm)	11	20	22

0, 1, 2, and 3. For an applied voltage of ±2.5 V, the value of the remnant polarization, $2P_r$, ranges between $10\,\mu C\,cm^{-2}$ for Sample 0 and $25\,\mu C\,cm^{-2}$ for Sample 2. Samples 1 and 3 show a $2P_r$ of 23, and $20\,\mu C\,cm^{-2}$, respectively. The $P-V$ curves indicate that the presence of the Ti layer increases the ferroelectric imprint, introducing a systematic left shift of the hysteresis loops of Samples 1, 2, and 3. In these cases, the Ti layer modifies the work function of the top electrode. This creates an asymmetry between the electrodes, which is responsible for a built-in field. This phenomenon has been already described in the literature for other ferroelectric-based stacks with different electrodes.[32] The obtained results show that the presence of the Ti layer clearly increases the value of $2P_r$. The highest $2P_r$ is obtained for Sample 2 and the lowest for Sample 0. This could be attributed to two factors: I) The chemical properties of the Ti/HZO interface, which are different from the ones of the interface TiN/HZO, promotes the formation of *o*-phase grains. The thermal expansion coefficient (TEC) of Ti and TiN have close values, 0.9410^{-5} and $0.810^{-5}\,K^{-1}$, respectively.[33,34] Because Ti and TiN TECs are similar, we propose that the main cause of ferroelectricity enhancement in HZO, in samples with Ti, could arise from the different chemical reconstructions of the top interface. II) The increased number of oxygen vacancies in HZO, which is induced by the Ti layer,[35] takes part in the stabilization of the orthorhombic phase in the HZO film.[36,37] For a thicker interfacial layer, the polarization inverts its rising, dropping to $20\,\mu C\,cm^{-2}$ for Sample 3. This behavior can be explained by the increasing depolarizing field produced at the interface by the TiO_z dielectric layer, which is responsible for the lower remnant polarization in Sample 3.[38,39] This tendency is also confirmed in the literature, Si et al.,[40] Qu et al.,[41] and Shekhawat et al.[11] have reported a suppression of the ferroelectricity when the thickness of the dielectric layer is increased. Furthermore, Samples 1, 2, and 3 show a positive $2P_r$ in the pristine state, contrary to the null value of Sample 0. This result is explained by the hypothesis that the interfacial properties of Ti/HZO promote the formation of *o*-phase crystallites. The endurance curves in Figure 7 show that $2P_r$ increases for Samples 1, 2, and 3 until breakdown occurs, while Sample 0 enters in a fatigue state after $\approx 10^6$ cycles, where $2P_r$ decreases to $\approx 9\,\mu C\,cm^{-2}$. The increase of the remnant polarization is associated to the well-known wake-up effect, which is partly due to the redistribution of the defects, typically oxygen vacancies, during the cycling process.[42,43] **Table 2** gives the value of the remnant polarization of Samples 0, 1, 2, and 3 in the pristine state, after 10^4 cycles, and before breakdown. **Figure 6** shows its trends as a function of the Ti thickness.

The endurance tests were performed on the four samples until breakdown. **Figure 7** shows the change of remnant polarization P_+ and P_- according to the applied number of voltage cycles. At 2.5 V, the value of $|P_+|$ and $|P_-|$ starts at $\approx 5\,\mu C\,cm^{-2}$ for Samples 1, 2, and 3, and at $\approx 0\,\mu C\,cm^{-2}$ in the case of Sample 0, for which it starts rising after 5×10^2 cycles. In Sample 0, P_r reaches its maximum after 10^5 cycles. For Samples 1, 2, and 3, P_r rises until breakdown, which occurs after 10^6, 5×10^5, and 10^7 cycles, respectively. On average, the obtained results indicate that the endurance value of the here tested devices is comparable to what is reported in the literature.[10,18]

From the analysis of the presented results, we formulated a hypothesis that could explain the obtained trends for P_r and endurance as a function of the thickness of the Ti layer. A 2 or 3 nm thick Ti interfacial layer, is enough to ensure the bulk-like chemistry of titanium and titanium oxide, favoring the *o*-phase formation through oxygen vacancy generation, and providing a higher remnant polarization. This is true in the case of the pristine state as well. The decrease of P_r of Sample 3 can be ascribed to the increased depolarizing field that is induced by a

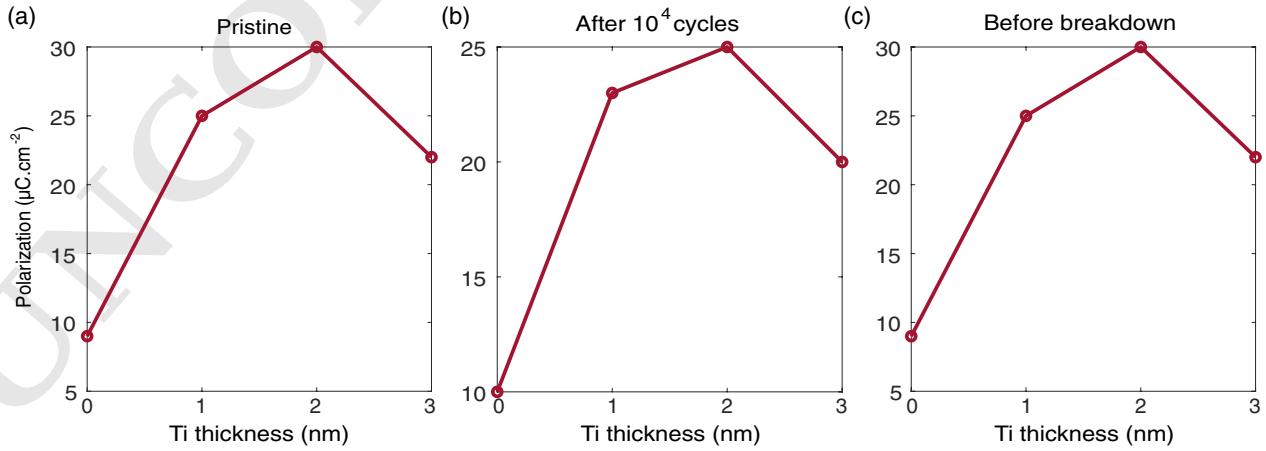

Figure 6. Remnant polarization versus Ti thickness for Samples 0, 1, 2, and 3, indicating the trend of $2P_r$ in: a) pristine state, b) after 10^4 cycles, c) before breakdown.

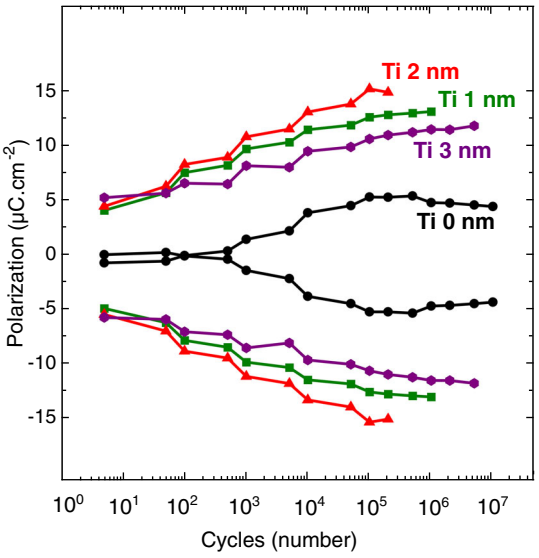

Figure 7. Electrical characterization of Samples 0, 1, 2, and 3: endurance tests.

thick dielectric layer. We can suppose that a 3 nm thick Ti layer is not as beneficial as a 2 nm thick one, as far as P_r is concerned. Furthermore, in Sample 1, the Ti layer is too thin to provide the same interface conditions as in Samples 2 and 3, and so to increase P_r at the value of Sample 2. This could be due to the fact that a 1 nm thick Ti layer is not enough to have the same chemical properties as bulk Ti. As mentioned, Ti scavenges oxygen from HZO, thus creating oxygen vacancies at the top interface. Besides stabilizing the ferroelectric phase at low HZO thickness, a high amount of oxygen vacancy is responsible for an increased leakage current that could make the specimen more fragile.[44] About the endurance, the highest value corresponds to Sample 0, which can be considered satisfying for a 6 nm thick HZO film. For Sample 1, we mentioned that the 1 nm thick Ti layer is not sufficient to increase P_r as for Sample 2. However, it might produce more oxygen vacancies that can impact the endurance, which decreases with respect to Sample 0. In Sample 3, a 3 nm thick Ti layer is sufficient to efficiently scavenge oxygen from the HZO film, but since the formed dielectric layer is thicker with respect to Samples 1 and 2, it might result in a more resistant sample than Samples 1 and 2. Eventually, for Sample 2, the chemical properties of the Ti/HZO interface promote the *o*-phase formation, and the Ti layer is thin enough to limit the effect of the depolarizing field, compared to Sample 3. Nevertheless, these benefits could be impacted by an enhanced fragility of the sample, where the increased number of oxygen vacancies is responsible for a breakdown after a low number of cycles.[44] The stacks containing the Ti layer can be compared to other structures reported in the literature, as shown in **Table 3**. The studies presented in Table 3 highlight that the insertion of an ultra-thin interfacial layer at one or both electrode/HZO interfaces is beneficial for the electrical properties of HZO-based devices. For instance, an ultra-thin interfacial layer improves the value of the remnant polarization of HZO by favoring the *o*-phase nucleation at low annealing temperatures, simplifying the integration of ferroelectric HZO into the CMOS process. Furthermore, it is helpful to enhance the tunnel electroresistance ratio for FTJ applications. Here, we demonstrate that the Ti layer is fundamental to improve the ferroelectricity of ultra-thin HZO films. We show an enhanced value of the remnant polarization in the pristine state for samples with Ti layer, which almost triples once the capacitors are cycled. This result makes the insertion of the interfacial layer a very promising approach to further scale down the thickness of ferroelectric HZO for FTJ devices. However, additional experiments are necessary to deeper investigate the electrical properties of the presented devices and the role of the interfacial layer. It would be of great interest to perform current versus voltage (I–V) measurements to explore the dominant conduction mechanisms inside the HZO film, capacitance versus voltage measurements (C–V) to probe the impact of the Ti interfacial layer, and the conductance method ($G_{p/\omega}$)[45] to evaluate the density of trap states at the dielectric/ferroelectric interface.[40,41]

Table 3. State of the art: thin-HZO-based structure with the addition of interfacial layers (ALD stands for atomic layer deposition, PE-ALD for plasma-enhanced ALD).

Reference	Structure	Fabrication method	HZO thickness [nm]	Interfacial layer thickness [nm]	$2P_r$ [μCcm^{-2}]	Endurance
Gaddam et al.[13]	TiN/TiO_2/HZO/HfO_2/TiN	PE-ALD	10	1	16	10^8
Shekhawat et al.[11]	p-Ge/Al_2O_3/HZO/TiN/Pt	ALD	8.4	1	15	10^5
				1.8	12	10^5
				2.2	7	between 10^5 and 10^6
Qi et al.[12]	Si/TiN/TiO_2/HZO/TiO_2/TiN	PE-ALD	10	2	8 (as deposited and after wake-up)	
Ryu et al.[14]	p-Si/HZO/Al_2O_3/Ti/Au	ALD	12	3	21	10^6
In this work	n^+Si/TiN/HZO/Ti/TiN/Ti/Pt	RF MS	6	1	23	10^6
				2	25	5×10^5
				3	20	10^7

4. Conclusion

The structural, compositional, and electrical characterizations of HZO-based stacks were performed by X-Ray diffraction, electron energy-loss spectroscopy, and PUND technique, respectively. The impact of a Ti interfacial layer of different thicknesses was investigated with the aim of optimizing the ferroelectric properties of thin HZO films for future ferroelectric tunnel junction applications. The results revealed that the Ti interfacial layer plays an important role in the microstructure and the electrical performances of HZO-based capacitors. The most promising structure is the one where a 2 nm thick Ti layer was inserted at the top electrode/HZO interface. This consideration is a tradeoff between, on the one hand, the chemistry of the Ti/HZO interface, and the induced oxygen redistribution that stabilizes the *o*-phase in HZO and, on the other hand, the effect of the depolarizing field that diminishes the value of the remnant polarization. The improvement of the electrical performances of HZO-based heterostructures by engineering the electrodes/HZO interfaces is a promising approach that can lead to a further scaling of these devices for nonvolatile memory applications.

Acknowledgements

This work was realized on the NanoLyon technology platform and on the Micro Nano Research Facility at RMIT University. It was funded by the European Union's Horizon 2020 research and innovation programme under Grant Agreement No. 780302 (3eFERRO), by the I3E ECLAUSion project that has received funding from the European Union's Horizon 2020 research and innovation programme under the Marie Skłodowska-Curie grant agreement No 801512, and by the French Public Authorities through the NANO 2022 program. The STEM-EELS work was performed at the *consortium Lyon-St-Etienne de microscopie*. The access to the facilities and technical support from the RMIT Microscopy and Microanalysis Facility, a linked laboratory of Microscopy, Australia, is acknowledged.

Conflict of Interest

The authors declare no conflict of interest.

Data Availability Statement

The data that support the findings of this study are available from the corresponding author upon reasonable request.

Keywords

ferroelectricity, HZO, thin films

Received: November 15, 2021
Revised: March 7, 2022
Published online:

[1] T. Böscke, J. Müller, D. Bräuhaus, U. Schröder, U. Böttger, in *2011 Int. Electron Devices Meeting*, IEEE, Piscataway, NJ **2011**, pp. 24–25.
[2] J. Müller, T. Böscke, D. Bräuhaus, U. Schröder, U. Böttger, J. Sundqvist, P. Kücher, T. Mikolajick, L. Frey, *Appl. Phys. Lett.* **2011**, *99*, 112901.
[3] S. Oh, H. Hwang, I. Yoo, *APL Mater.* **2019**, *7*, 091109.
[4] J. Muller, T. S. Boscke, U. Schroder, S. Mueller, D. Brauhaus, U. Bottger, L. Frey, T. Mikolajick, *Nano Lett.* **2012**, *12*, 4318.
[5] M. H. Park, H. J. Kim, Y. J. Kim, Y. H. Lee, T. Moon, K. D. Kim, S. D. Hyun, F. Fengler, U. Schroeder, C. S. Hwang, *ACS Appl. Mater. Interfaces* **2016**, *8*, 15466.
[6] V. Garcia, M. Bibes, *Nat. Commun.* **2014**, *5*, 1.
[7] L. Chen, T.-Y. Wang, Y.-W. Dai, M.-Y. Cha, H. Zhu, Q.-Q. Sun, S.-J. Ding, P. Zhou, L. Chua, D. W. Zhang, *Nanoscale* **2018**, *10*, 15826.
[8] E. Tsymbal, A. Gruverman, *Nat. Mater.* **2013**, *12*, 602.
[9] F. Ambriz-Vargas, G. Kolhatkar, R. Thomas, R. Nouar, A. Sarkissian, C. Gomez-Yáñez, M. Gauthier, A. Ruediger, *Appl. Phys. Lett.* **2017**, *110*, 093106.
[10] B. Max, M. Hoffmann, S. Slesazeck, T. Mikolajick, in *2018 48th European Solid-State Device Research Conference (ESSDERC)*, IEEE, Piscataway, NJ **2018**, pp. 142–145.
[11] A. Shekhawat, G. Walters, N. Yang, J. Guo, T. Nishida, S. Moghaddam, *Nanotechnology* **2020**, *31*, 39LT01.
[12] Y. Qi, X. Xu, I. Krylov, M. Eizenberg, *Appl. Phys. Lett.* **2021**, *118*, 032906.
[13] V. Gaddam, D. Das, T. Jung, S. Jeon, *IEEE Electron Device Lett.* **2021**, *42*, 812.
[14] H. Ryu, H. Wu, F. Rao, W. Zhu, *Sci. Rep.* **2019**, *9*, 1.
[15] M. H. Park, H. J. Kim, Y. J. Kim, Y. H. Lee, T. Moon, K. D. Kim, S. D. Hyun, C. S. Hwang, *Appl. Phys. Lett.* **2015**, *107*, 192907.
[16] J. Bouaziz, P. Rojo Romeo, N. Baboux, B. Vilquin, *J. Vac. Sci. Technol. B* **2019**, *37*, 021203.
[17] J. Bouaziz, P. Rojo Romeo, N. Baboux, R. Negrea, L. Pintilie, B. Vilquin, *APL Mater.* **2019**, *7*, 081109.
[18] J. Bouaziz, P. R. Romeo, N. Baboux, B. Vilquin, *ACS Appl. Electron. Mater.* **2019**, *1*, 1740.
[19] Y. H. Lee, H. J. Kim, T. Moon, K. Do Kim, S. D. Hyun, H. W. Park, Y. B. Lee, M. H. Park, C. S. Hwang, *Nanotechnology* **2017**, *28*, 305703.
[20] K. He, N. Chen, C. Wang, L. Wei, J. Chen, *Cryst. Res. Technol.* **2018**, *53*, 1700157.
[21] Y. Kihn, C. Mirguet, L. Calmels, *J. Electron Spectrosc. Relat. Phenom.* **2005**, *143*, 117.
[22] F. Esaka, K. Furuya, H. Shimada, M. Imamura, N. Matsubayashi, H. Sato, A. Nishijima, A. Kawana, H. Ichimura, T. Kikuchi, *J. Vac. Sci. Technol. A* **1997**, *15*, 2521.
[23] F. M. F. de Groot, J. C. Fuggle, B. T. Thole, G. A. Sawatzky, *Phys. Rev. B* **1990**, *41* 928.
[24] T. Mizoguchi, M. Saitoh, Y. Ikuhara, *J. Phys.: Conden. Matter* **2009**, *21*, 104212.
[25] D. W. McComb, *Phys. Rev. B* **1996**, *54*, 7094.
[26] S. S. Cheema, D. Kwon, N. Shanker, R. Dos Reis, S.-L. Hsu, J. Xiao, H. Zhang, R. Wagner, A. Datar, M. R. McCarter, C. R. Serrao, A. K. Yadav, G. Karbasian, C.-H. Hsu, A. J. Tan, L.-C. Wang, V. Thakare, X. Zhang, A. Mehta, E. Karapetrova, R. V. Chopdekar, P. Shafer, E. Arenholz, C. Hu, R. Proksch, R. Ramesh, J. Ciston, S. Salahuddin, *Nature* **2020**, *580*, 478.
[27] G. Wilk, D. Muller, *Appl. Phys. Lett.* **2003**, *83*, 3984.
[28] S. Ramanathan, D. A. Muller, G. D. Wilk, C. M. Park, P. C. McIntyre, *Appl. Phys. Lett.* **2001**, *79*, 3311.
[29] J. H. Jang, H.-S. Jung, J. H. Kim, S. Y. Lee, C. S. Hwang, M. Kim, *J. Appl. Phys.* **2011**, *109*, 023718.
[30] S. Ostanin, A. Craven, D. McComb, D. Vlachos, A. Alavi, M. Finnis, A. Paxton, *Phys. Rev. B* **2000**, *62*, 14728.
[31] D.-Y. Cho, H.-S. Jung, C. S. Hwang, *Phys. Rev. B* **2010**, *82*, 094104.

[32] J. Wang, M. D. Nguyen, N. Gauquelin, J. Verbeeck, M. T. Do, G. Koster, G. Rijnders, E. Houwman, *Phys. Status Solidi RRL* **2020**, *14*, 1900520.
[33] P. Hidnert, *J. Res. Natl. Bur. Stand* **1943**, *30*, 101.
[34] E. Mohammadpour, M. Altarawneh, J. Al-Nu'airat, Z.-T. Jiang, N. Mondinos, B. Z. Dlugogorski, *Mol. Simul.* **2018**, *44*, 415.
[35] D. Walczyk, T. Bertaud, M. Sowinska, M. Lukosius, M. Schubert, A. Fox, D. Wolansky, A. Scheit, M. Fraschke, G. Schoof, et al., in *2012 Int. Semiconductor Conf. Dresden-Grenoble (ISCDG)*, IEEE, Piscataway, NJ **2012**, pp. 143–146.
[36] T. Mittmann, M. Materano, S.-C. Chang, I. Karpov, T. Mikolajick, U. Schroeder, in *2020 IEEE Int. Electron Devices Meeting (IEDM)*, IEEE, Piscataway, NJ **2020**, pp. 18–4.
[37] T. Mittmann, M. Michailow, P. D. Lomenzo, J. Gärtner, M. Falkowski, A. Kersch, T. Mikolajick, U. Schroeder, *Nanoscale* **2021**, *13*, 912.
[38] S. Oh, H. Kim, A. Kashir, H. Hwang, *Appl. Phys. Lett.* **2020**, *117*, 252906.
[39] P. D. Lomenzo, S. Slesazeck, M. Hoffmann, T. Mikolajick, U. Schroeder, B. Max, in *2019 19th Non-Volatile Memory Technology Symp. (NVMTS)*, IEEE, Piscataway, NJ **2019**, 1–8.
[40] M. Si, X. Lyu, P. D. Ye, *ACS Appl. Electron. Mater.* **2019**, *1*, 745.
[41] Y. Qu, J. Li, M. Si, X. Lyu, D. Y. Peide, *IEEE Trans. Electron Dev.* **2020**, *67*, 5315.
[42] H. J. Kim, M. H. Park, Y. J. Kim, Y. H. Lee, T. Moon, K. Do Kim, S. D. Hyun, C. S. Hwang, *Nanoscale* **2016**, *8*, 1383.
[43] Y.-J. Lin, C.-Y. Teng, S.-J. Chang, Y.-F. Liao, C. Hu, C.-J. Su, Y.-C. Tseng, *Appl. Surf. Sci.* **2020**, *528*, 147014.
[44] D. R. Islamov, V. A. Gritsenko, T. V. Perevalov, V. A. Pustovarov, O. M. Orlov, A. G. Chernikova, A. M. Markeev, S. Slesazeck, U. Schroeder, T. Mikolajick, et al., *Acta Mater.* **2019**, *166*, 47.
[45] E. Nicollian, A. Goetzberger, *Bell Syst. Tech. J.* **1967**, *46*, 1055.

physica status solidi rrl
rapid research letters

By providing the payment information below, you agree that you are responsible for the charges and taxes (as applicable), and that you will promptly pay the invoice in accordance with the terms thereof.

Reprint Order Form

Please complete this form and return it via E-Mail to the Editorial Office.
E-mail: pss.rapid@wiley-vch.de

Manuscript No.: _____
Customer No.: (if available) _____
Purchase Order No.: _____
Author: _____

Charges for Reprints in Euro (excl. VAT), prices are subject to change. Minimum order 50 copies

No. of pages	50 copies	100 copies	150 copies	200 copies	300 copies	500 copies
1– 4	345,—	395,—	425,—	445,—	548,—	752,—
5– 8	490,—	573,—	608,—	636,—	784,—	1077,—
9–12	640,—	739,—	786,—	824,—	1016,—	1396,—
13–16	780,—	900,—	958,—	1004,—	1237,—	1701,—
17–20	930,—	1070,—	1138,—	1196,—	1489,—	2022,—
every additional 4 pages	147,—	169,—	175,—	188,—	231,—	315,—

Information regarding VAT: The charges for publication of *cover pictures /reprints/issues/poster/Video abstracts/* are considered to be "supply of services" and therefore subject to German VAT. However, if you are an institutional customer outside Germany, the tax can be waived if you provide us with the valid VAT number of your company. Non-EU customers may have a VAT number starting with "EU" instead of their country code, if they are registered with the EU tax authorities. If you do not have a valid EU VAT number and you are a taxable person doing business in a non-EU country, please provide a certification from your local tax authorities confirming that you are a taxable person under local tax law. Please note that the certification must confirm that you are a taxable person and are conducting an economic activity in your country. **Note:** certifications confirming that you are a tax-exempt legal body (non-profit organization, public body, school, political party, etc.) in your country do not exempt you from paying German VAT.

Please send me send bill me for

☐ no. of reprints

☐ high-resolution PDF file (330 Euro excl. VAT)
E-mail address: _____

❖ Special Offer:

If you order 200 or more reprints you will get a PDF file for half price.

Please note: It is not permitted to present the PDF file on the internet or on company homepages.

Cover Posters (prices excl. VAT)
Posters of published covers are available in two sizes:

☐ DIN A2 42 x 60 cm / 17 x 24in (one copy: 39 Euro)

☐ DIN A1 60 x 84 cm / 24 x 33in (one copy: 49 Euro)

Postage for shipping (prices excl. VAT)
overseas +25 Euro
within Europe +15 Euro

_____
Date, Signature

VAT number: _____

Mail reprints / copies of the issue to:

_____
_____
_____
_____
_____

Send bill to:

_____
_____
_____
_____

☐ **I will pay by bank transfer**

☐ **I will pay by credit card**

VISA, Mastercard and AMERICAN EXPRESS

For your security please use this link (Credit Card Token Generator) to create a secure code Credit Card Token and include this number in the form instead of the credit card data. Click here:
https://www.wiley-vch.de/editorial_production/index.php

CREDIT CARD TOKEN NUMBER

						V									

Wiley-VCH GmbH– A company of John Wiley & Sons, Inc. -
Location of the Company: Weinheim - Trade Register: Mannheim, HRB 736569
Managing Directors: Sabine Haag und Guido Herrmann

WILEY-VCH